RAA 2020 Vol. **20** No. **9**, 146(15pp) doi: 10.1088/1674–4527/20/9/146

http://www.raa-journal.org *http://iopscience.iop.org/raa*

Research in Astronomy and Astrophysics

Estimating the power spectrum of a discrete cosmic momentum field with fast Fourier transform

Jun Pan

National Astronomical Observatories, Chinese Academy of Sciences, Beijing 100101, China; *jpan@bao.ac.cn*

Received 2019 November 24; accepted 2020 April 16

Abstract Fast Fourier transform based estimators are formulated for measuring momentum power spectra, including the auto power spectra of the momentum, the momentum divergence, and the cross spectrum of density fluctuation and momentum divergence. Algorithms using the third order Bettle-Lemarié scaling function to assign discrete objects to regular grids for fast Fourier transform are proposed to clean alias effects. Numerical experiments prove that the implementation can achieve sub-percent precision till close to the Nyquist frequency. The impact of removing bulk flow on the estimation of momentum power spectra is derived theoretically and verified numerically. Subtracting bulk flow has little effects at large scales but might induce meaningful differences in nonlinear regime, and probably it is not necessary to subtract bulk flow for samples which peculiar velocities are exact or sufficiently accurate. Momentum power spectra of dark matter samples from N-body simulation are measured and discussed. As expected, the prediction of the one loop Eulerian perturbation theory agrees with simulation only slightly better than the linear theory at $z = 0$, but can be applied to higher redshift with improved accuracy. Measurements of simulation data and the one loop Eulerian theory both reveal that the momentum field contains strong rotational part, and there is a large stochastic component in the divergence of momentum which is not correlated with the density field. The three kinds of momentum power spectra have their own characteristics.

Key words: large scale structure of Universe — cosmology: theory — methods: numerical — methods: statistical

1 INTRODUCTION

The cosmic momentum, as a product of the dimensionless density and the peculiar velocity, is essentially the core of velocity correlation functions (e.g., Gorski et al. 1989; Wang et al. 2018) and the kinematic Sunyaev-Zel'dovich effect (kSZ, e.g., Ma & Fry 2002; Park et al. 2016). There is also a strong link between the divergence of cosmic momentum and the Rees-Sciama effect (e.g., Seljak 1996) and the integrated Sachs-Wolfe effect (ISW, e.g., Smith et al. 2009). Much attention has been paid to realize the potential of momentum power spectrum in cosmology, including an attempt to develop theoretical models (e.g, Okumura et al. 2014; Carrasco et al. 2014; Senatore & Zaldarriaga 2015; Sugiyama et al. 2016) and practices of probing the physical Universe (Park 2000; Park & Park 2006; Qin et al. 2019).

To facilitate research on cosmic momentum, reliable and accurate algorithms to estimate power spectrum of cosmic momentum is pivotal. One of the benefit of working with momentum is that there is not such an annoying uneven sampling problem as in the analysis of the volume-weighted peculiar velocity field. If it is the volume-weighted velocity field to be explored, special algorithms have to be devised to resample the peculiar velocity field, such as algorithms implemented with Delaunay or Voronoi tessellation (e.g., Bernardeau & van de Weygaert 1996; Pueblas & Scoccimarro 2009), or interpolation based on various kernel functions (e.g., Colombi et al. 2007; Zheng et al. 2013; Yu et al. 2015). Even armed with these tools, accuracy control is yet very challenging to the estimation of statistics of volume-limited velocity fields, which actually varies by case. In contrast, the algorithm of measuring momentum spectrum effectively is similar to that of the density power spectrum, as already shown by Park (2000), Park & Park (2006) and Howlett (2019). In these works, estimators for the momentum power spectrum accounting for shot noises and proper weights, are proposed and tested, setting up a solid basis for relevant applications. However, if fast Fourier transform (hereafter

FFT) is adopted to realize these algorithms, the alias effect could be significant (Jing 2005), where treatment is absent in current procedures.

Meanwhile it is worth addressing that the momentum and the momentum divergence are different. The cosmic momentum is mainly related to applications about correlation functions of peculiar velocities, while the momentum divergence is connected to cosmological probes about the temporal evolution of gravitational potential. The momentum field is composed of its potential and curl components, mathematically it is quite simple to take the spatial derivative of the momentum field to generate its divergence, but numerically measuring the power spectrum of momentum divergence would require a different estimator which is not explicitly presented. Thereof the main purpose of this report is to present a formal derivation and description of FFT-based estimators of the auto power spectra of the cosmic momentum field, momentum divergence and the cross spectrum of density and momentum divergence, with an appropriate prescription for cleaning shot noise and aliasing effect. As it is straightforward to apply these algorithms to non-uniform samples, estimators presented here are about ideal samples free of effects of selection functions, geometric masking and etc.

In the next section, we will present algorithms for the estimation of power spectra of momentum. Section 3 is dedicated to investigation on effects of subtracting bulk flow, momentum spectra of dark matter samples of a N-body simulation are explored in Section 4. The last section is of discussion and conclusion.

2 ESTIMATORS

2.1 Auto Power Spectrum of the Cosmic Momentum

At a given position $\boldsymbol{r}$, the cosmic momentum of dark matter or structures like halos or galaxies, is defined by

$$\boldsymbol{p}(\boldsymbol{r}) \equiv (1+\delta(\boldsymbol{r}))\,\boldsymbol{v}(\boldsymbol{r}) \tag{1}$$

with δ being the number density contrast and $\boldsymbol{v}$ the peculiar velocity. For a sample of volume V_S, in Fourier space at wave vector $\boldsymbol{k}$ the momentum can be written in analogues to a vector,

$$\begin{aligned}\boldsymbol{p}(\boldsymbol{k}) &\equiv \frac{1}{V_S}\int \boldsymbol{p}(\boldsymbol{r})e^{i\boldsymbol{k}\cdot\boldsymbol{r}}\mathrm{d}\boldsymbol{r}\\ &= \frac{1}{V_S}\int (\mathrm{p}_{\hat{e}_1}(\boldsymbol{r}),\ \mathrm{p}_{\hat{e}_2}(\boldsymbol{r}),\ \mathrm{p}_{\hat{e}_3}(\boldsymbol{r}))\,e^{i\boldsymbol{k}\cdot\boldsymbol{r}}\mathrm{d}\boldsymbol{r}\\ &= (\mathrm{p}_{\hat{e}_1}(\boldsymbol{k}),\ \mathrm{p}_{\hat{e}_2}(\boldsymbol{k}),\ \mathrm{p}_{\hat{e}_3}(\boldsymbol{k}))\ ,\end{aligned} \tag{2}$$

the momentum power spectrum is constructed by

$$P_p(\boldsymbol{k}) = \langle \boldsymbol{p}(\boldsymbol{k})\cdot\boldsymbol{p}^*(\boldsymbol{k})\rangle = \sum_{j=1}^{3}\langle \mathrm{p}_{\hat{e}_j}(\boldsymbol{k})\mathrm{p}^*_{\hat{e}_j}(\boldsymbol{k})\rangle, \tag{3}$$

where the supscript $*$ refers to the complex conjugate, $\hat{e}_j$ is one of the three unit coordinate vectors defining a three-dimensional Cartesian coordinate system.

Shot noise can be derived following Peebles (1980, sect. 41). The sample space V_S is divided into infinitesimal cells of volume $\mathrm{d}V_{S,j}$ in which number of objects $n_j = 1$ or 0, and if $n_j = 1$ there is measurement of peculiar velocity $\boldsymbol{v}_j$. Let $\sum_j n_j = N$ and $\bar{n} = \langle n_j\rangle = N/V_S$,

$$\hat{\boldsymbol{p}}(\boldsymbol{k}) = \frac{1}{N}\sum_j n_j\boldsymbol{v}_j e^{i\boldsymbol{k}\cdot\boldsymbol{r}_j}\ , \tag{4}$$

and

$$\begin{aligned}\langle \hat{\boldsymbol{p}}(\boldsymbol{k}_1)\cdot\hat{\boldsymbol{p}}^*(\boldsymbol{k}_2)\rangle = &\frac{1}{N^2}\sum_{j,\ell,j\neq\ell}\langle (n_j\boldsymbol{v}_j)\cdot(n_\ell\boldsymbol{v}_\ell)\rangle e^{i\boldsymbol{k}_1\cdot\boldsymbol{r}_j - i\boldsymbol{k}_2\cdot\boldsymbol{r}_\ell}\\ &+\frac{1}{N^2}\sum_j\langle n_j^2v_j^2\rangle e^{i(\boldsymbol{k}_1-\boldsymbol{k}_2)\cdot\boldsymbol{r}_j}\ .\end{aligned} \tag{5}$$

Since $n_j = 1$ or 0, $n_j^2 = n_j = 1$ or 0, replacing the ensemble average with spatial averages yields

$$\begin{aligned}&\langle n_j^2v_j^2\rangle = \sum_{j,n_j=1} v_j^2/N \equiv \hat{\sigma}_v^2\,,\\ &\langle (n_j\boldsymbol{v}_j)\cdot(n_\ell\boldsymbol{v}_\ell)\rangle_{j\neq\ell} = \bar{n}^2\xi_p(\boldsymbol{r}_2-\boldsymbol{r}_1)\mathrm{d}V_{S,j}\mathrm{d}V_{S,\ell}\ ,\end{aligned} \tag{6}$$

where $\xi_p = \langle \boldsymbol{p}(\boldsymbol{r}_1)\cdot\boldsymbol{p}(\boldsymbol{r}_2)\rangle$ is the scalar two-point correlation function of cosmic momentum. The raw power spectrum turns to be as simple as

$$\hat{P}_p(\boldsymbol{k}) = P_p(\boldsymbol{k}) + \frac{\hat{\sigma}_v^2}{N}\ . \tag{7}$$

The aliasing effect is formulated with the approach of Jing (2005). The sampling function corresponding to grids for FFT is a sum of Dirac functions $\Pi(\boldsymbol{r}/\Delta L) \equiv \sum_{\boldsymbol{J}}\delta_D(\boldsymbol{r}/\Delta L - \boldsymbol{J})$ in which $\boldsymbol{J}$ is an integer vector and ΔL is the grid spacing. Let the window function used to assign objects to grid points be W, the raw momentum becomes $\hat{\boldsymbol{p}}(\boldsymbol{r}) = \Pi\left(\boldsymbol{r}/\Delta L\right)\int \boldsymbol{p}(\boldsymbol{r}_1)W(\boldsymbol{r}_1-\boldsymbol{r})\mathrm{d}\boldsymbol{r}_1$ so that

$$\hat{\boldsymbol{p}}(\boldsymbol{k}) = \frac{1}{N}\int \Pi\left(\frac{\boldsymbol{r}}{\Delta L}\right)\sum_j n_j\boldsymbol{v}_j W(\boldsymbol{r}_j-\boldsymbol{r})e^{i\boldsymbol{k}\cdot\boldsymbol{r}}\mathrm{d}\boldsymbol{r}\ , \tag{8}$$

and the power spectrum would be constructed through

$$\begin{aligned}\langle \hat{\boldsymbol{p}}(\boldsymbol{k}_1)\cdot\hat{\boldsymbol{p}}^*(\boldsymbol{k}_2)\rangle = &\frac{1}{N^2}\\ &\times\int\int \mathrm{d}\boldsymbol{r}_1\mathrm{d}\boldsymbol{r}_2\Pi\left(\frac{\boldsymbol{r}_1}{\Delta L}\right)\Pi\left(\frac{\boldsymbol{r}_2}{\Delta L}\right)e^{i(\boldsymbol{k}_1\cdot\boldsymbol{r}_1-\boldsymbol{k}_2\cdot\boldsymbol{r}_2)}\\ &\times\left[\sum_{j,\ell,j\neq\ell}\langle (n_j\boldsymbol{v}_j)\cdot(n_\ell\boldsymbol{v}_\ell)\rangle W(\boldsymbol{r}_j-\boldsymbol{r}_1)W(\boldsymbol{r}_\ell-\boldsymbol{r}_2)\right.\\ &\left.+\sum_j\langle n_j^2\boldsymbol{v}_j^2\rangle W(\boldsymbol{r}_j-\boldsymbol{r}_1)W(\boldsymbol{r}_j-\boldsymbol{r}_2)\right]\ .\end{aligned} \tag{9}$$

Since

$$\begin{aligned}\Pi(\boldsymbol{k}) &= \frac{1}{V_s}\int \Pi\left(\frac{\boldsymbol{r}}{\Delta L}\right) e^{i\boldsymbol{k}\cdot\boldsymbol{r}}\mathrm{d}\boldsymbol{r} \\ &= \frac{(2\pi)^3}{V_s}\sum_{\boldsymbol{J}}\delta_D(\boldsymbol{k}-2k_N\boldsymbol{J})\end{aligned} \tag{10}$$

with $k_N = \pi/\Delta L$ being the Nyquist frequency, there is the raw momentum power spectrum

$$\begin{aligned}\hat{P}_p(\boldsymbol{k}) =& P_p(\boldsymbol{k})W^2(\boldsymbol{k}) \\ &+ \sum_{\boldsymbol{J}\neq 0} W^2(\boldsymbol{k}+2k_N\boldsymbol{J})P_p(\boldsymbol{k}+2k_N\boldsymbol{J}) \\ &+ \frac{\hat{\sigma}_v^2}{N}\sum_{\boldsymbol{J}} W^2(\boldsymbol{k}+2k_N\boldsymbol{J}) \,,\end{aligned} \tag{11}$$

which is very similar to the formula of matter power spectrum in Jing (2005) except for a factor $\hat{\sigma}_v^2$ topped on the shot noise term, correction methods of Jing (2005), Cui et al. (2008), Yang et al. (2009) and Colombi et al. (2009) all can be readily applied.

2.2 Auto Power Spectrum of the Momentum Divergence

The momentum divergence $\theta_p \equiv -\nabla\cdot\boldsymbol{p}(\boldsymbol{r})/(Haf)$ in Fourier space is $\theta_p(\boldsymbol{k}) = i\boldsymbol{k}\cdot\boldsymbol{p}(\boldsymbol{k})/(Haf)$, $f = \mathrm{d}\log D(a)/\mathrm{d}\log a$ and $D(a)$ is the linear density growth factor at redshift $z = 1/a - 1$. Practically, divergence of momentum field is produced through $\hat{\theta}_p(\boldsymbol{k}) = i\boldsymbol{k}\cdot\hat{\boldsymbol{p}}(\boldsymbol{k})/(Haf)$, such that

$$\begin{aligned}\hat{P}_{\theta_p}(\boldsymbol{k}) &= \langle\hat{\theta}_p\hat{\theta}_p^*\rangle \\ &= \frac{1}{(Haf)^2}\langle[\boldsymbol{k}\cdot\hat{\boldsymbol{p}}(\boldsymbol{k})]\,[\boldsymbol{k}\cdot\hat{\boldsymbol{p}}^*(\boldsymbol{k})]\rangle \,.\end{aligned} \tag{12}$$

Inserting Equation (8) results in

$$\begin{aligned}\hat{P}_{\theta_p}(\boldsymbol{k}) =& \; P_{\theta_p}(\boldsymbol{k})W^2(\boldsymbol{k}) \\ &+ \frac{1}{(Haf)^2}\sum_{\boldsymbol{J}\neq 0} W^2(\boldsymbol{k}+2k_N\boldsymbol{J}) \\ &\quad \langle[\boldsymbol{k}\cdot\boldsymbol{p}(\boldsymbol{k}+2k_N\boldsymbol{J})][\boldsymbol{k}\cdot\boldsymbol{p}^*(\boldsymbol{k}+2k_N\boldsymbol{J})]\rangle \\ &+ \frac{k^2}{(Haf)^2}\frac{\langle v^2\mu^2\rangle}{N}\sum_{\boldsymbol{J}} W^2(\boldsymbol{k}+2k_N\boldsymbol{J}) \,,\end{aligned} \tag{13}$$

where $\langle v^2\mu^2\rangle = \sum_j v_j^2\mu_j^2/N$ with $\mu_j = \boldsymbol{k}\cdot\boldsymbol{v}_j/(kv_j)$.

The shot noise in Equation (13) deserves more attention. For a fair sample, such as a full simulation data, the condition $\sum_j \boldsymbol{v}_j = 0$ tells that $\sum v_j\mu_j = 0$. By virtue of isotropy and homogeneity, velocity amplitude v shall not be correlated with its direction μ, thus $\langle v^2\mu^2\rangle = \hat{\sigma}_v^2\langle\mu^2\rangle$, and $1/3$ could be a convenient approximation to $\langle\mu^2\rangle$. But for samples constructed from observation of a finite space of the Universe, or extracted as subsamples of the full simulation, the bulk flow $\boldsymbol{v}_b = \sum_j \boldsymbol{v}_j/N$ is generally not zero, the shot noise will be directional dependent. To see the point, let $\boldsymbol{v}' = \boldsymbol{v} - \boldsymbol{v}_b$, $\mu' = \boldsymbol{k}\cdot\boldsymbol{v}'/(kv')$ and $\mu_b = \boldsymbol{k}\cdot\boldsymbol{v}_b/(kv_b)$, such that

$$\langle v^2\mu^2\rangle = \langle v'^2\mu'^2\rangle + v_b^2\mu_b^2 = \hat{\sigma}_{v'}^2\langle\mu'^2\rangle + v_b^2\mu_b^2 \,, \tag{14}$$

in which $\hat{\sigma}_{v'}^2 = \sum_{j=1}^N(\boldsymbol{v}_j - \boldsymbol{v}_b)^2/N$. Obviously the shot noise varies with μ_b, and the strength of such dependence is determined by amplitude of v_b. Of course, in isotropic $P_{\theta_p}(k)$, the $\boldsymbol{k}$ directional dependence of shot noise vanishes and $\langle v^2\mu^2\rangle = \sigma_v^2/3$.

2.3 Cross Spectrum of the Density and the Momentum Divergence

It is fairly trivial to construct the estimator for the cross spectrum, in analogues to the last subsection,

$$\begin{aligned}\hat{P}_{\delta\theta_p}(\boldsymbol{k}) =& P_{\delta\theta_p}(\boldsymbol{k})W^2(\boldsymbol{k}) \\ &- \frac{i}{Haf}\sum_{\boldsymbol{J}\neq 0} W^2(\boldsymbol{k}+2k_N\boldsymbol{J}) \\ &\quad \langle\delta(\boldsymbol{k}+2k_N\boldsymbol{J})\,[\boldsymbol{k}\cdot\boldsymbol{p}^*(\boldsymbol{k}+2k_N\boldsymbol{J})]\rangle \\ &- \frac{ik}{Haf}\frac{\langle v\mu\rangle}{N}\sum_{\boldsymbol{J}} W^2(\boldsymbol{k}+2k_N\boldsymbol{J}) \,.\end{aligned} \tag{15}$$

It is easy to see that $\langle v\mu\rangle = v_b\mu_b$, an interesting thing is that non-zero bulk flow induces shot noise in the imaginary part of the cross spectrum, and such shot noise will be zero in the isotropic power spectrum $P_{\delta\theta_p}(k)$.

2.4 Test with N-body Simulation Data

2.4.1 Algorithm setup and data preparation

FFT is computed with the FFTW3 package (Frigo & Johnson 2005). Assignment of objects to FFT grids is implemented with the third-order orthogonalized Battle-Lemarié spline function (Yang et al. 2009), practice shows that the adoption of the fifth-order B-spline function brings up minute differences less than 1%.

Samples used for our experiments are produced from data sets of a N-body simulation. The simulation is of pure dark matter and realized with the *Gadget-2* code (Springel 2005), which assumes a Λ cold dark matter (ΛCDM) cosmology model with parameters $\Omega_m = 0.26$, $\Omega_b = 0.044$, $\Omega_\Lambda = 0.74, h = 0.71$, $\sigma_8 = 0.8$, $n_s = 1$. The run consists of $N = 1024^3$ particles within a periodic cubic box of size $L_{\mathrm{box}} = 1000\ h^{-1}$ Mpc, each particle has mass of $6.72\times 10^{10}\ h^{-1}M_\odot$. Samples employed in this work include

1. outputs of the simulation at picked redshifts, mainly the one at $z = 0$ and the initial condition at $z = 80$;

2. ten random samples generated from the $z = 0$ output by randomly relocating dark matter particles while preserving their velocities both in amplitude and direction.
3. two sets of 64 subsamples at $z = 0$ and $z = 80$ respectively, constructed by evenly splitting the full sample volume into $4 \times 4 \times 4$ non-overlapping cubes of size 250 Mpc h^{-1}.

2.4.2 *Shot noise*

Models of shot noise are checked with the ten random samples at $z = 0$. The randomization procedure erase any non-trivial correlations among density and velocity, their raw power spectra are simply signals of shot noise. Meanwhile as only particle positions are changed, σ_v^2 and $\langle v^2\mu^2\rangle$ are kept invariant, and $v_b = 0$. In the experiment, the nearest grid point (NGP) method is used to assign objects to FFT grids, as for uniformly random samples NGP method is exact (Jing 2005). We did compare results using the third order Bettle-Lemarié scaling function, in general the resulting random fluctuation is less than 1%, whilst the systematic difference is around 0.4% when k becomes close to Nyquist frequency.

Comparison between measurements and models are presented in Figure 1, it clearly indicates that performance of models is satisfactory, except that fluctuation of measured shot noise in cross-spectrum is larger than others. In order to test effects of bulk flow on shot noise, an artificial bulk flow of $v_b = 341$ km s^{-1} is added to the random samples along particular direction, and then power spectra are measured for comparison. By Figure 1, it is clear that the shot noise models are indeed working very well.

2.4.3 *Aliasing*

Aliasing effects in the power spectra are checked with the dark matter sample at $z = 0$ of N-body simulation, the third order Bettle-Lemarié scaling function is adopted to assign objects upon FFT grids. As there is no *true* power spectra as a template for comparison, power spectra are estimated with different resolutions of FFT grids, then measurements of low FFT resolutions are compared with those of higher FFT resolutions (Fig. 2). It appears that the performance of the algorithm is fairly satisfactory, the consistency indicates that for k scales below the Nyquist frequency k_N the aliasing damping to the power spectrum is tiny:

- the k scale above which deviations are larger than 1% are about $0.87k_N$, $0.82k_N$, $0.74k_N$ and $0.85k_N$ for P_p, P_{θ_p}, $P_{\delta\theta_p}$ and P_δ respectively;
- at scales $k \leq 0.7k_N$ precision of 0.5% can be ensured, while at scale of $0.5k_N$, the relative differences are less than 0.2%;
- even when k is very close k_N relative differences are generally less than 5%.

As a reference, if NGP is used for object assignment, scales where difference is larger than 1% are $\sim 0.12k_N$ for these power spectra, the aliasing damping is much more severe.

3 IMPACT OF SUBTRACTING BULK FLOW

In the previous section the influence of non-zero bulk flow on the shot noises of the momentum power spectra has been analyzed. However effects of non-zero bulk flow could be more than the simple modulation to shot noises. Park & Park (2006) noticed the problem, and Howlett (2019) carried out extensively numerical exploration with mock catalogues, they conjectured that removing the bulk flow from measured peculiar velocities brings little changes to power spectra, but are reminded that in practical works it should be tested case by case. In this section we will mainly focus on the changes after subtracting bulk flow from peculiar velocities to the estimated momentum power spectra.

3.1 Momentum

Since aliasing can be well corrected in our algorithms, in the following derivation we will not include aliasing effects any longer. In the case of the bulk flow $\boldsymbol{v}_b = \sum_j \boldsymbol{v}_j/N \neq 0$, it is always possible to define a new velocity by removing the bulk flow $\boldsymbol{v}' = \boldsymbol{v} - \boldsymbol{v}_b$ to generate a new momentum field $\boldsymbol{p}' = \boldsymbol{p} - (1+\delta)\boldsymbol{v}_b$ with zero bulk flow. The raw power spectrum of the new momentum field is

$$\widehat{P}_{p'}(\boldsymbol{k}) = \frac{1}{N^2}\sum_{j\neq\ell}\langle(n_j\boldsymbol{v}'_j)\cdot(n_\ell\boldsymbol{v}'_\ell)\rangle e^{i\boldsymbol{k}\cdot(\boldsymbol{r}_j-\boldsymbol{r}_\ell)} + \frac{\hat{\sigma}^2_{v'}}{N}\,, \tag{16}$$

where shot noise is related to Equation (6) through

$$\hat{\sigma}_v^2 = \sum_{j,n_j=1} v'^2_j/N + v_b^2 = \hat{\sigma}^2_{v'} + v_b^2\,. \tag{17}$$

Correlation functions in Equations (5) and (16) are linked by

$$\begin{aligned}\langle n_j\boldsymbol{v}_j\cdot n_\ell\boldsymbol{v}_\ell\rangle_{j\neq\ell} = &\langle n_j\boldsymbol{v}'_j\cdot n_\ell\boldsymbol{v}'_\ell\rangle_{j\neq\ell}\\ &+ v_b\langle n_jn_\ell(v'_j\eta'_j + v'_\ell\eta'_\ell)\rangle_{j\neq\ell}\\ &+ v_b^2\langle n_jn_\ell\rangle_{j\neq\ell}\,,\end{aligned} \tag{18}$$

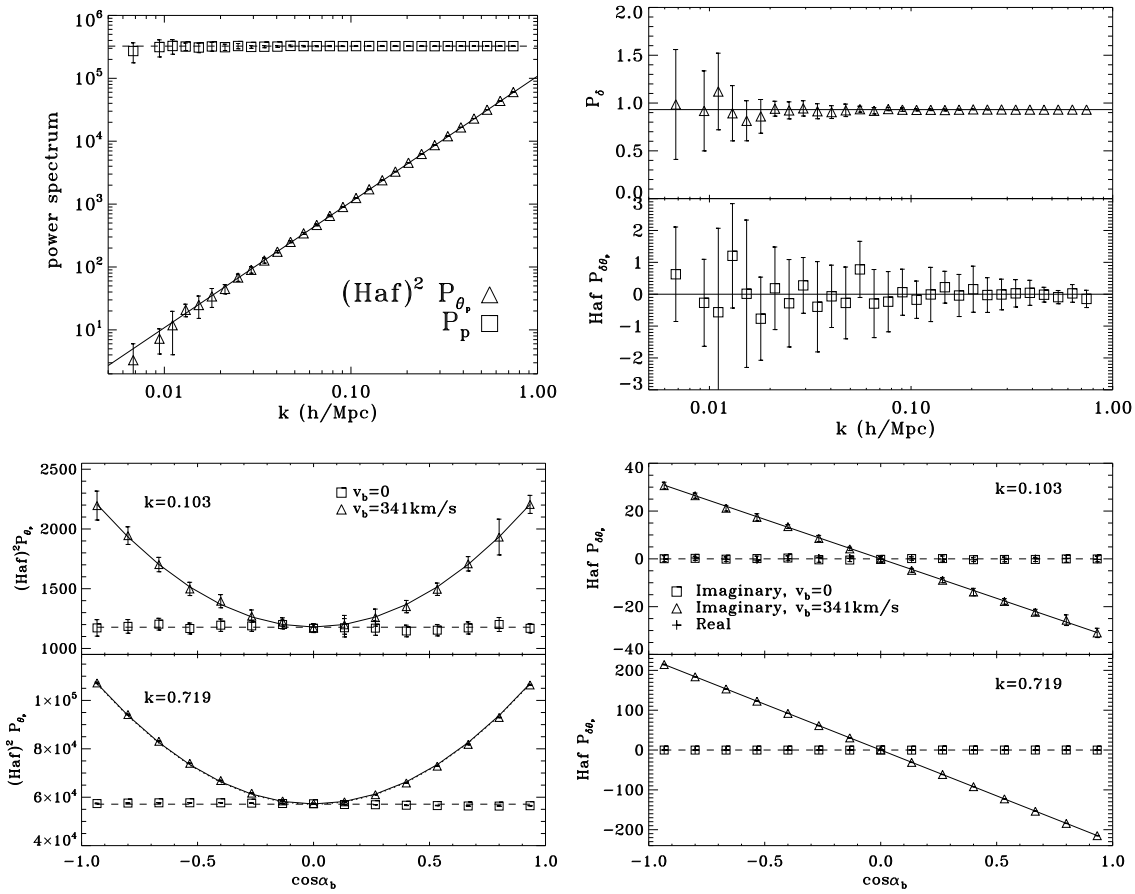

Fig. 1 Raw power spectra of random samples, displayed as test of shot noise models. Symbols are averages of ten random samples, error bars are their standard deviations, *lines* are the expectation of shot noise models. α_b is the angle between bulk flow $\boldsymbol{v}_b$ and wave vector $\boldsymbol{k}$. Random samples with non-zero bulk flow are created by adding a flow of $v_b = 341\ \mathrm{km\,s^{-1}}$ along particular direction.

in which $v'_j = \left|\boldsymbol{v}'_j\right|$, $v_b = |\boldsymbol{v}_b|$ and $\eta'_j = \boldsymbol{v}'_j \cdot \boldsymbol{v}_b/(v'_j v_b)$. Note that there is the correspondence

$$\begin{aligned}
\langle (n_j \boldsymbol{v}_j)\cdot(n_\ell \boldsymbol{v}_\ell)\rangle_{j\neq\ell} &\leftrightarrow P_p(\boldsymbol{k})\,,\\
\langle (n_j \boldsymbol{v}'_j)\cdot(n_\ell \boldsymbol{v}'_\ell)\rangle_{j\neq\ell} &\leftrightarrow P_{p'}(\boldsymbol{k})\,,\\
\langle n_j n_\ell (v'_j\eta'_j + v'_\ell\eta'_\ell)\rangle_{j\neq\ell} &\leftrightarrow P_{\delta p'_b}(\boldsymbol{k}) + P_{\delta p'_b}(-\boldsymbol{k})\,,\\
\langle n_j n_\ell\rangle_{j\neq\ell} &\leftrightarrow P(\boldsymbol{k})\,,
\end{aligned} \tag{19}$$

where $P(\boldsymbol{k}) = \langle \delta(\boldsymbol{k})\delta^*(\boldsymbol{k})\rangle$, $P_{\delta p'_b}(\boldsymbol{k}) = \langle \delta(\boldsymbol{k}) p'^*_b(\boldsymbol{k})\rangle$, $p'_b(\boldsymbol{k})$ is the Fourier transform of $p'_b(\boldsymbol{r}) = \rho\boldsymbol{v}'\cdot\boldsymbol{v}_b/v_b = \rho v'\eta'$, finally there is the relation

$$\begin{aligned}
P_p(\boldsymbol{k}) = P_{p'}(\boldsymbol{k}) &+ v_b\left[P_{\delta p'_b}(\boldsymbol{k}) + P^*_{\delta p'_b}(\boldsymbol{k})\right]\\
&+ v_b^2 P(\boldsymbol{k})\,.
\end{aligned} \tag{20}$$

In a practical application, P_p and $P_{p'}$ can be estimated via a Equation (11), $P(\boldsymbol{k})$ can be measured through $\widehat{P}(\boldsymbol{k}) = P(\boldsymbol{k}) + 1/N$, while $\widehat{P}_{\delta p'_b} = P_{\delta p'_b}$.

3.2 Momentum Divergence

The quantity implemented in the algorithm to estimate statistics of momentum divergence is constructed by

$$\hat{\theta}_p(\boldsymbol{k}) = \frac{1}{N}\sum_j \frac{i\boldsymbol{k}}{Haf}\cdot(n_j\boldsymbol{v}_j)e^{i\boldsymbol{k}\cdot\boldsymbol{r}_j}\,. \tag{21}$$

If $v_b \neq 0$, with $\mu_b = \boldsymbol{k}\cdot\boldsymbol{v}_b/(kv_b)$, there are

$$\begin{aligned}
&\langle[i\boldsymbol{k}\cdot(n_j\boldsymbol{v}_j)][-i\boldsymbol{k}\cdot(n_\ell\boldsymbol{v}_\ell)]\rangle_{j\neq\ell}\\
&= \langle[i\boldsymbol{k}\cdot(n_j\boldsymbol{v}'_j)][-i\boldsymbol{k}\cdot(n_\ell\boldsymbol{v}'_\ell)]\rangle_{j\neq\ell}\\
&\quad + ikv_b\mu_b\langle n_j[-i\boldsymbol{k}\cdot(n_\ell\boldsymbol{v}'_\ell)] - [i\boldsymbol{k}\cdot(n_j\boldsymbol{v}'_j)]n_\ell\rangle_{j\neq\ell}\\
&\quad + k^2v_b^2\mu_b^2\langle n_j n_\ell\rangle_{j\neq\ell}\langle n_j[-i\boldsymbol{k}\cdot(n_\ell\boldsymbol{v}_\ell)]\rangle_{j\neq\ell}\\
&= \langle n_j[-i\boldsymbol{k}\cdot(n_\ell\boldsymbol{v}'_\ell)]\rangle_{j\neq\ell} - ikv_b\mu_b\langle n_j n_\ell\rangle_{j\neq l}\,.
\end{aligned} \tag{22}$$

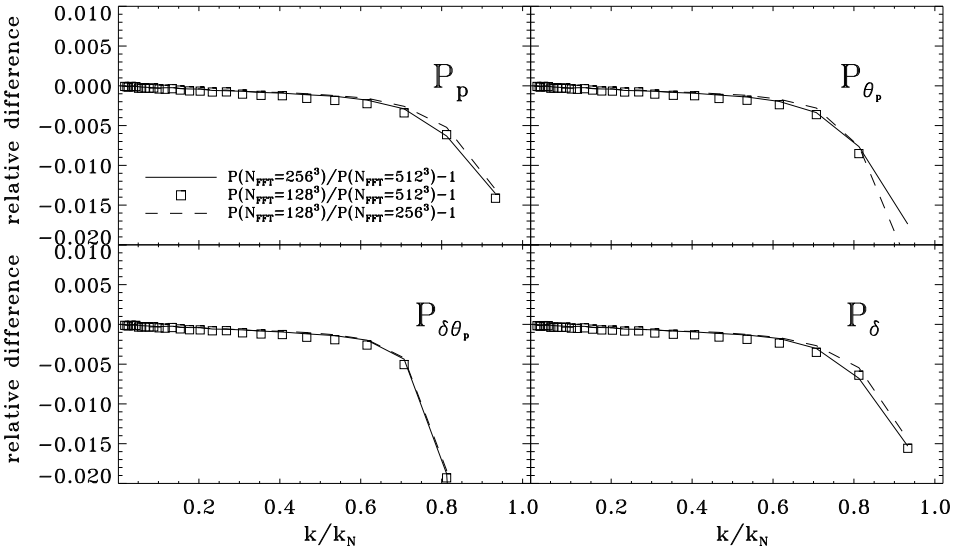

Fig. 2 Aliasing effects in power spectra of dark matter at $z = 0$ which object assignment upon FFT grids is realized with the third order Bettle-Lemarié scaling function. $N_{\rm FFT}$ is the number of grids used for FFT, k_N is the Nyquist frequency of the measurement of lower FFT resolution in each pair of power spectra for comparison.

Subsequently if we let the divergence of momentum after subtracting $\boldsymbol{v}_b$ be θ'_p, we obtain the following equations,

$$\begin{aligned} P_{\theta_p}(\boldsymbol{k}) &= P_{\theta'_p}(\boldsymbol{k}) + ik\mu_b \frac{v_b}{Haf}[P_{\delta\theta'_p}(\boldsymbol{k}) - P^*_{\delta\theta'_p}(\boldsymbol{k})] \\ &\quad + k^2\mu_b^2 \left(\frac{v_b}{Haf}\right)^2 P(\boldsymbol{k})\,, \\ P_{\delta\theta_p}(\boldsymbol{k}) &= P_{\delta\theta'_p}(\boldsymbol{k}) - ik\mu_b \frac{v_b}{Haf} P(\boldsymbol{k})\,. \end{aligned} \tag{23}$$

P_{θ_p}, $P_{\theta'_p}$, $P_{\delta\theta_p}$ and $P_{\delta\theta'_p}$ can be measured by Equations (13) and (15) respectively.

3.3 Numerical Experiments

It is well-known that bulk flow of a sample follows Maxwellian distribution

$$\mathcal{P}(v_b)\mathrm{d}v_b = \sqrt{\frac{2}{\pi}}\left(\frac{3}{\sigma^2_{v_b}}\right)^{3/2} v_b^2 \exp\left(-\frac{3v_b^2}{2\sigma^2_{v_b}}\right)\mathrm{d}v_b, \tag{24}$$

which is solely controlled by the variance $\sigma^2_{v_b} = \int P_{\boldsymbol{v}}\widetilde{W}_S^2 d^3k/(2\pi)^3$, $\widetilde{W}_S$ is the window function defining the sample space in Fourier space (e.g., Bahcall et al. 1994; Li et al. 2012). Usually the sample space is sufficiently large to approximate the mass-weighted velocity power spectrum $P_{\boldsymbol{v}}$ with the linear power spectrum of density fluctuation P_L by $(Haf/k)^2 P_L$. The most likely speed of bulk flow is $\sqrt{2/3}\sigma_{v_b}$, the mean $\langle v_b\rangle = \sqrt{8/(3\pi)}\sigma_{v_b}$ and the mean square speed $\langle v_b^2\rangle = \sigma^2_{v_b}$. The characteristic speed of bulk flow corresponding to the volume of our simulation is $\sigma_{v_b} = 51.5$ km s^{-1}, so an artificial bulk flow $v_b = \sigma_{v_b}$ in an arbitrary selected direction is added to the dark matter sample at $z = 0$ of the simulation to form a sample with non-zero bulk flow, then power spectra are estimated to check the resulting influence. Summary of our experiments is shown in Figure 3. Equations (20) and (23) are confirmed with excellent accuracy (better than 0.03%), even the statistical fluctuations due to the limited number of modes at large scales are recovered perfectly.

It is apparent that the modulation depends on the amplitude of v_b, major contribution comes from $v_b^2 P$, at large scales $P_p \sim (Haf)^2 k^{-2} P$, the relative difference $P_p/P_{p'} - 1$ is roughly $k^2 v_b^2/(Haf)^2 \sim 4(v_b/100)^2 k^2$ at $z \sim 0$. If sample volume is large, the chance to have a large bulk flow is relatively small, it is expected that P_p at large scales will not change significantly by subtracting the bulk flow, but at small scales one might have to consider the difference, as shown in the left panel of Figure 4. An important issue one has to bear in mind, what is presented in Figure 4 is of dark matter. If at large scales $k <\sim 0.1\ h$ Mpc^{-1}, peculiar velocities of biased objects such as galaxies are only slightly biased with respect to the dark matter, i.e., $b_v \approx 1$ (Chen et al. 2018), the correction to the momentum power spectra of galaxies after removing bulk flow will be actually boosted by the square of the galaxy density bias parameter.

A serious question is whether $\boldsymbol{p}$ or $\boldsymbol{p}'$ should be used to estimate the power spectra. Non-zero monople of peculiar velocities can also emerge by systematics in peculiar velocity estimation methods, i.e., the velocity zero point offsets which might have distinct distribution function from

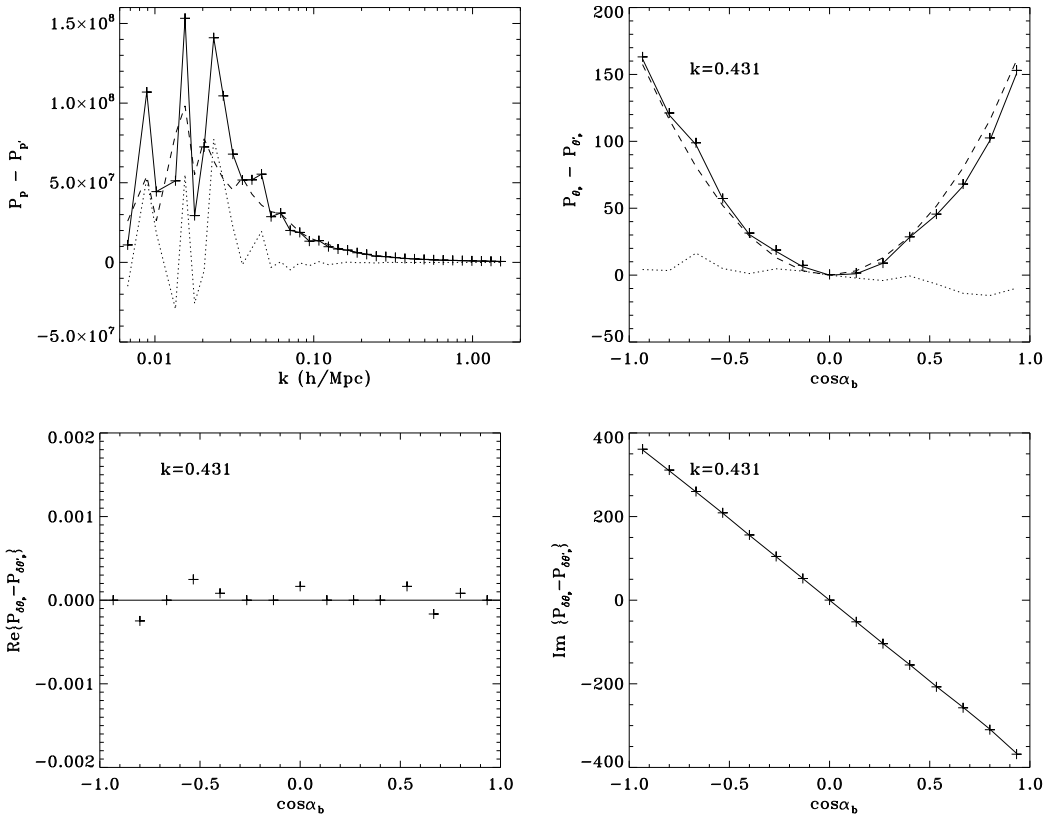

Fig. 3 Differences in measured momentum power spectra after removing bulk flow. An artificial bulk flow of speed $v_b = 51.5$ km s^{-1} is added to the $z = 0$ realization of the simulation to create a sample with bulk flow, $\alpha_b = \cos^{-1}\mu_b$ is the angle between $\boldsymbol{k}$ and $\boldsymbol{v}_b$. *Top left*: *cross symbols* are $P_p - P_{p'}$, the *solid line* is $v_b(P_{\delta p'_b} + P^*_{\delta p'_b}) + v_b^2 P$, *dotted line* is $v_b(P_{\delta p'_b} + P^*_{\delta p'_b})$, and *dashed line* is $v_b^2 P$ (Eq. (20)). *Top right crosses* are $P_{\theta_p} - P_{\theta'_p}$, *solid line* is $ik\mu_b(P_{\delta\theta'_p} - P^*_\delta)v_b/(Haf) + k^2\mu_b^2(v_b/Haf)^2 P$ in which the first term is drawn in *dotted line* and the second term is the *dashed line* (Eq. (23)). *Bottom left*: *crosses* are the real part of $P_{\delta\theta_p} - P_{\delta\theta'_p}$, *solid line* is the expectation of zero. *Bottom right*: the imaginary part of $P_{\delta\theta_p} - P_{\delta\theta'_p}$, *solid line* is $-k\mu_b(v_b/Haf)P$ (Eq. (23)).

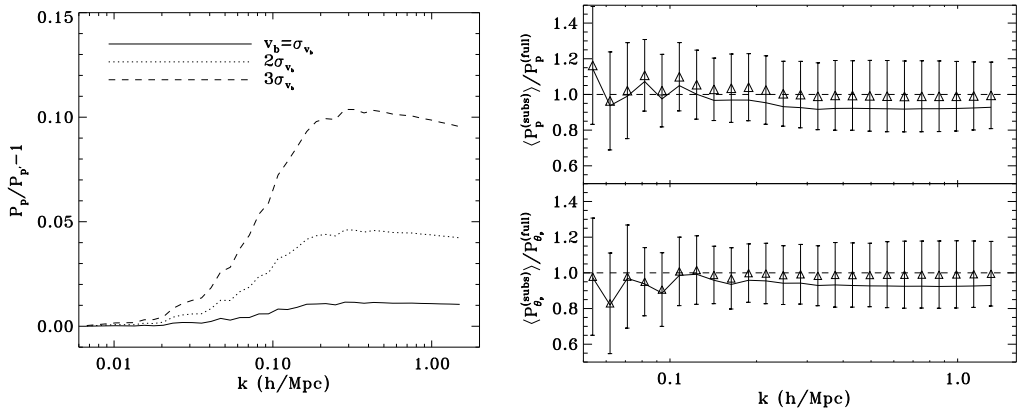

Fig. 4 *Left panel*: differences in P_p after removing bulk flows of different amplitudes, $\sigma_{v_b} = 51.5$ km s^{-1}. *Right panel*: differences between averages of power spectra of the 64 subsamples and power spectra of the full sample; *triangles* are averages of the power spectra of the subsample without removing their bulk flows, error bars are their standard deviations; *solid lines* are the averages of the subsamples' power spectra with their bulk flows subtracted; *dashed horizontal lines* are the reference lines of 1.

the intrinsic flow. If the measured bulk flow is caused by the peculiar velocity zero point offset alone, no doubt that one needs to deduct the measured bulk flow directly. If peculiar velocities are given exactly, such as in samples constructed from simulation data, the bulk flow is purely intrinsic, it is then another story. In order to clarify the point, the power spectra of our 64 subsamples at $z = 0$ are estimated with and without their particular bulk flow subtracted respectively. Then averages of these power spectra are compared with the measurements of the sample of full size to check possible systematical biases. As expected by Equations (20) and (23) after replacing v_b^2 with $\sigma^2_{v_b}$, we can see from the right panel of Figure 4, where subtracting bulk flows from the subsamples gives rise to systematically biased estimation of P_p and P_{θ_p} at small scales, although such biases seem not so significant against the fairly large dispersions among the measured momentum power spectra of subsamples. Nevertheless it appears that there is no need to subtract the bulk flow in this case. Measured bulk flow of real samples contains mingled contributions from both of the intrinsic flow and the velocity zero point offsets, one might have to inspect the strengths of the two sources carefully case by case.

4 MOMENTUM POWER SPECTRA OF DARK MATTER IN THE ΛCDM SIMULATION

4.1 At Large Scales

As an application, momentum power spectra of dark matter in the ΛCDM simulation at many epochs from the initial time of $z = 80$ to $z = 0$ are estimated with our algorithms. The measured power spectra of the full simulation are shown in Figure 5, it looks that linear theory matches simulations at large scales well, but the scale ranges allowed by the simulation for accuracy examination are very narrow, the box size of our simulation is 1 Gpc h^{-1} which in Fourier space corresponds to $k \approx 0.006$, the strong fluctuation at large scales in power spectra caused by a limited number of Fourier modes becomes an obstacle to observe the actual performance of theories.

Considering that we have only one simulation at hand, we estimated error bars as the standard deviation of the measurements of the 64 subsamples of the $z = 0$ output used in the last section, the shortcoming of this method is that since the box size of subsamples is only one quarter of the original full sample, error bars below $k <\sim 0.025$ are missing in our application thereof. We can see that uncertainties at large scales $k <\sim 0.1\ h\ \mathrm{Mpc}^{-1}$ are quite large (left panel of Fig. 6), which is known to be roughly inversely proportional to the square root of numbers of Fourier modes. Variances of momentum power spectra are persistently several times stronger than that of density power spectrum at $k >\sim 0.1$ h, being around 20% of P_p and P_{θ_p}, ∼10% of $P_{\delta\theta_p}$.

To assess precision of theoretical models, the object quantities estimated from the simulation should contains stochastic fluctuation as little as possible, overlaying error bars on the estimated power spectra only indicate a range of uncertainties, a method able to suppress sample variance would be very helpful. We realize that at very large scales, coupling among Fourier modes is in fact weak, Fourier modes can be deemed evolving linearly, such that data sets at later epochs actually maintain approximately the same large scale stochastic fluctuations as the random setup in the initial condition. We take the measured power spectra of the initial field granted as the linear templates, which differ from linear theoretical models by less than 2% if ignoring the cosmic variance. Thereafter using these linear templates to normalize measured power spectra at later times shall be able to alleviate cosmic variances.

To check the conjecture, power spectra of the 64 subsamples of the initial condition at $z = 80$ are then measured and linearly evolved to redshift $z = 0$, forming the class of linear templates denoted as $P^{(z=80)}$. Uncertainties are then estimated for power spectra normalized by these linear templates. The technique is indeed very effective, dramatically reduces the cosmic variances at large scales $k < 0.1\ h\,\mathrm{Mpc}^{-1}$ (Fig. 6), and relative uncertainties in momentum power spectra drop to ∼20% and become much stable. Comparison of linear theories with the measurements of simulation is displayed in Figure 7, the advantage of using the measured initial power spectra as a linear prediction is obvious, results are much smooth and convergent.

4.2 Beyond Linear Regime

It is not an easy task to predict nonlinear P_p, all nonlinear polyspectra on the right hand side of Equation (A.4) are needed, among which however only the nonlinear matter power spectrum over large scale range can be provided with good precision by either empirical fitting formulae (Smith et al. 2003; Takahashi et al. 2012) or halo model (e.g., Ma & Fry 2000; Scoccimarro et al. 2001). At large scales where nonlinearity is weak one could resort to the perturbative approach, such as the standard Eulerian perturbation theory (SPT, Appendix B). The one loop approximation of SPT on momentum power spectra (details in Appendix A) is compared with simulation results in Figure 8. The one loop SPT brings minor improvement over linear theory for the case of $z = 0$, but could be applied to slightly deeper scales at high redshifts $z > 1$ if the precision requirement is as moderate as 5%∼10%.

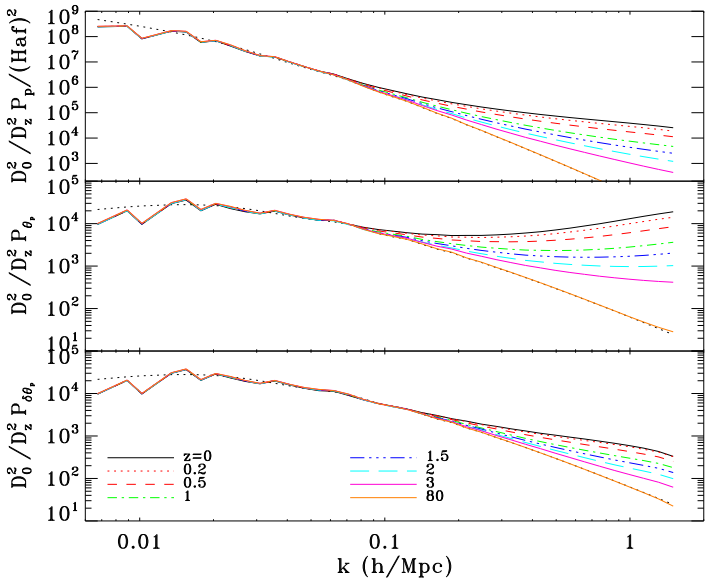

Fig. 5 Power spectra of dark matter in our ΛCDM simulation at selected redshifts from $z = 0$ to the simulation's starting epoch $z = 80$, *black dotted lines* which are almost coincident with the measurements at $z = 80$ are of the linear theory.

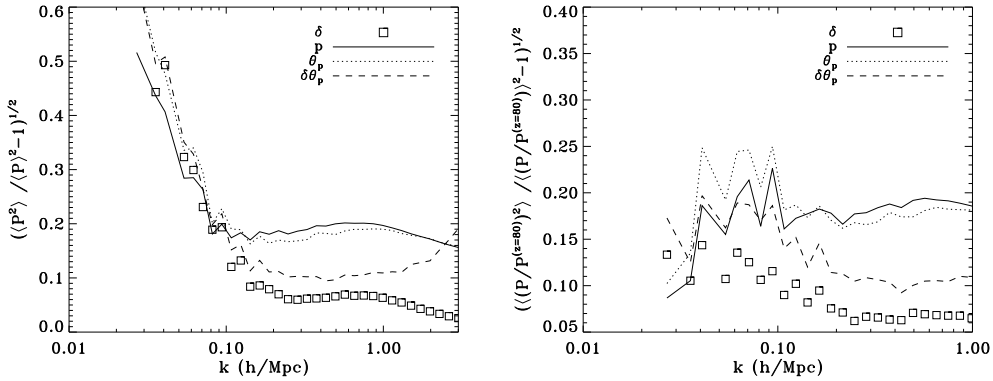

Fig. 6 *Left*: relative uncertainties in power spectra of dark matter at $z = 0$, being the normalized standard deviations among measurements of 64 subsamples, which are also the relative uncertainties of the ratios of power spectra to the linear theory. *Right*: the relative uncertainties of $P/P^{(z=80)}$, P refers to power spectrum of the specific kind at $z = 0$, $P^{(z=80)}$ is the linear template as the power spectrum estimated from the corresponding subsample extracted from the initial field (at $z = 80$) and linearly evolved to $z = 0$.

The one loop SPT is the simplest among perturbation theories. In principle there is no real obstacle in adopting other theories advanced in recent years. As a lengthy but incomplete list, there are the renormalized perturbation theory (e.g., Crocce & Scoccimarro 2006a,b, 2008; Bernardeau et al. 2008), the closure theory (Taruya & Hiramatsu 2008; Hiramatsu & Taruya 2009), the renormalization group perturbation theory (e.g., McDonald 2007; Matarrese & Pietroni 2007, 2008), and many other variants to these new techniques (e.g., Valageas 2008; Pietroni 2008; Pietroni et al. 2012; Bernardeau et al. 2012; Crocce et al. 2012; Anselmi & Pietroni 2012; Taruya et al. 2012; Sugiyama & Futamase 2012a,b). There are numerical codes implementing some of these novel approaches made available to the public, for example, the **CLASS**[1] (Lesgourgues 2011), the **RegPT**[2] (Taruya et al. 2012) and the **MPTbreeze**[3] (Crocce et al. 2012). Development of momentum spectra in theories at SPT beyond 1-loop level is beyond the scope of this paper, but an intrinsic shortcoming of these perturbation theories is their ignorance of velocity vorticity, which is likely the reason that these theories can not go deep into

[1] http://class-code.net

[2] http://www-utap.phys.s.u-tokyo.ac.jp/~ataruya/regpt_code.html

[3] http://maia.ice.cat/crocce/MPTbreeze/

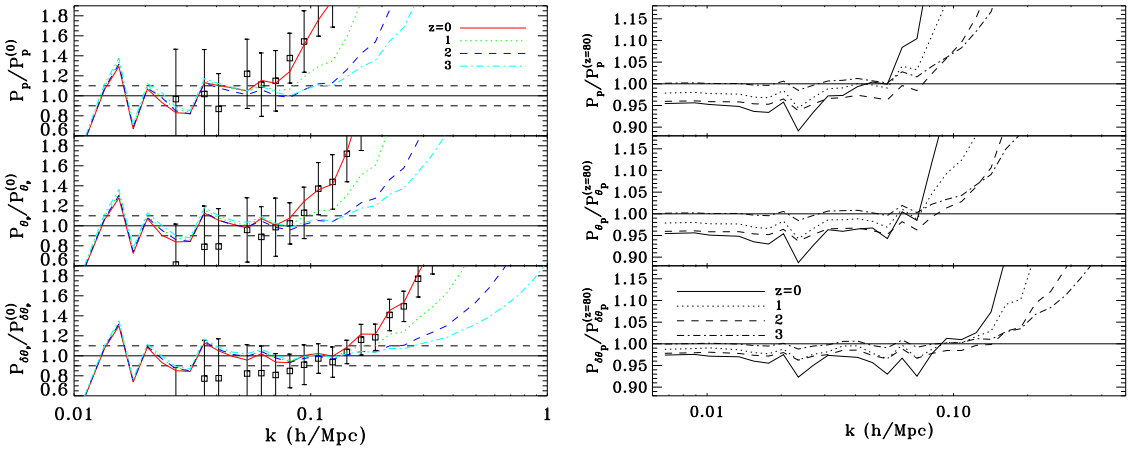

Fig. 7 *Left panel*: ratios of power spectra measured from simulation to the linear theory, *square symbols* are the averages of the 64 subsamples while error bars are corresponding standard deviations, *solid horizontal lines* are the unity ratio and the *dashed horizontal lines* delimit the 10% deviation; linear theory predicts that $P_p^{(0)} = D_z^2(Haf/k)^2 P_0$, $P_{\theta_p}^{(0)} = P_{\delta\theta_p}^{(0)} = D_z^2 P_0$, P_0 is the theoretical linear density power spectrum scaled to $z = 0$. *Right panel*: measured power spectra of the full sample, after normalization by linear templates.

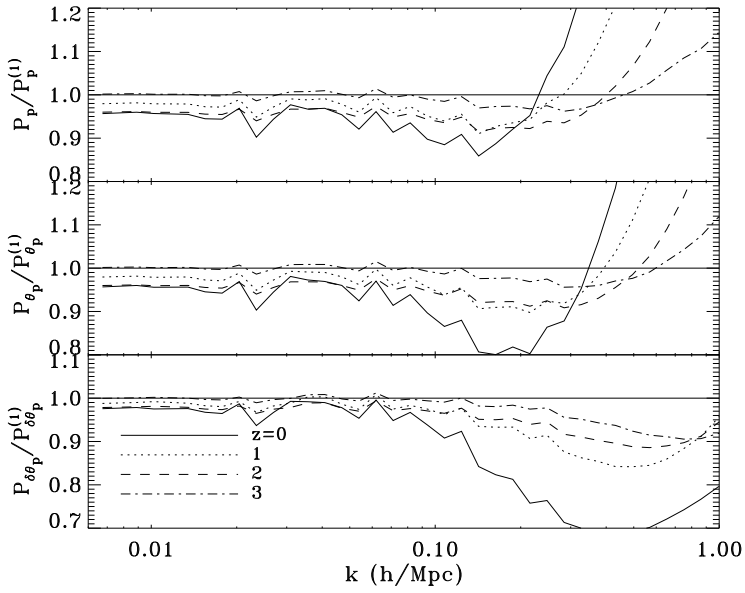

Fig. 8 Comparison of simulation with SPT at one loop level. To reduce sample variance, measured power spectra are normalized by $P^{(z=80)}$, theoretical power spectra $P^{(1)}$ are normalized by $P^{(0)}$ as well. $P_p^{(1)}$ is given by Eq. (A.7), $P_{\theta_p}^{(1)}$ and $P_{\delta\theta_p}^{(1)}$ are calculated with Eq. (A.11).

the nonlinear regime. We notice that a recently developed semi-analytical theory, namely the effective field theory (EFT), could recover the nonlinear evolution of statistics beyond stream crossing of the cosmic large scale structures much effectively (e.g., Carrasco et al. 2012; Baldauf et al. 2015; Foreman et al. 2016), which is a practical solution to fulfill the demand on theory of the precision cosmology.

At large scales it is often assumed that the curl component of peculiar velocity field is negligible, in principle one can reconstruct the vector velocity field from the its divergence field. But such operation is not applicable to the momentum field. The vorticity of momentum contains a component produced by the coupling between the spatial gradient of the density and the peculiar velocity,

$$\nabla \times \boldsymbol{p} = (1+\delta)\nabla \times \boldsymbol{v} + \nabla\delta \times \boldsymbol{v}\,. \qquad (25)$$

Obviously even if $\nabla \times \boldsymbol{v} = 0$ as assumed generally in perturbation theories, $\nabla \times \boldsymbol{p} \neq 0$, and the P_p is not equivalent

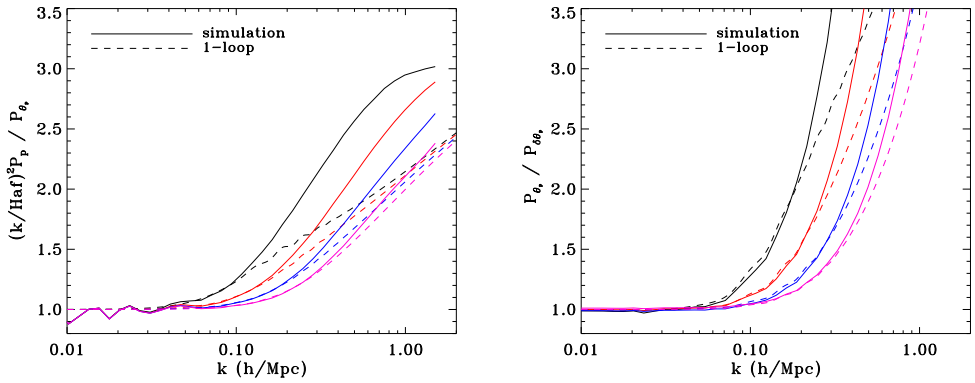

Fig. 9 Differences between P_p, P_{θ_p} and $P_{\delta\theta_p}$ at four epochs of $z = 0, 1, 2, 3$ (in colors of *black*, *red*, *blue* and *magenta* correspondingly) respectively. *Dashed lines* are the prediction of Eulerian perturbation theory at one loop level (details in Appendix A).

to P_{θ_p} at all (left panel of Fig. 9). The rotational part in momentum in simulation indeed becomes very strong already in a weakly nonlinear regime (Fig. 9). Eulerian perturbation theory at one loop (Appendix A) is invoked to check against simulation, the theory can only recover P_p/P_{θ_p} at $z = 0$ at scales $k < 0.1\ h$ Mpc^{-1}. We can see that even in perturbation theory, the relation between the momentum and its divergence is complicated, actually we tried several empirical proposals, but it seems there are no simple ways to recover P_p from P_{θ_p}.

Momentum divergence can be decomposed as the sum of two parts, namely a part θ_p^δ which is fully correlated with density fluctuation while the other one θ_p^S is not at all, $\theta_p = \theta_p^\delta + \theta_p^S$. The cross correlation $P_{\delta\theta_p}$ is effectively $\langle\delta\theta_p^\delta\rangle$, which does not contain any information of θ_p^S. As illustrated in the right panel of Figure 9, the power of θ_p^S is very large. We notice that $P_{\delta\theta_p} = \frac{1}{2f}\partial P_\delta/\partial\ln a$ is the time derivative of density power spectrum (Eq. (A.9)), thus it is viable to straightforwardly derive the nonlinear $P_{\delta\theta_p}$ of dark matter from the nonlinear matter power spectrum produced either by halo models (Cooray & Sheth 2002; Giocoli et al. 2010) or empirical formulas (Smith et al. 2003; Takahashi et al. 2012; Mead et al. 2015). The bad news is that, as we attempted, there is no such simple scaling relation between $P_{\theta_p^S}$ and $P_{\theta_p^\delta}$ as the one between P_{θ^δ} and P_{θ^S} found in Zheng et al. (2013). One has to search for new ways to establish a link between nonlinear P_{θ_p} and $P_{\delta\theta_p}$.

5 DISCUSSION AND CONCLUSION

In this report we present FFT-based estimators for auto power spectra of momentum and momentum divergence, and the cross spectrum of density fluctuation and momentum divergence. Although these estimators are for the ideal sample free of observational effects, which nevertheless can be readily incorporated to proposals handling with realistic observational samples. Algorithms to clean alias effects using the third order Bettle-Lemarié scaling function are proposed and thoroughly tested with simulation data sets; the experiment proves that the algorithm is able to preserve sub-percent precision till close to the Nyquist frequency.

It is pointed out that non-zero bulk flow could induce additional shot noises, but that is only part of the story. Bulk flow might induce much more complicated effects as already discussed in Park & Park (2006) and Howlett (2019). Exact formulas are derived and numerically confirmed to depicting the changes caused by removing bulk flow from peculiar velocities. Subtracting bulk flow results in generally minuscule changes to momentum power spectra at large scales, but might has non-negligible significance in the nonlinear regime. Interestingly the real part of $P_{\delta\theta_p}$ is immune to bulk flow. Numerical experiment suggests that there is no need to subtract bulk flow from peculiar velocities for samples whose peculiar velocities are exact or estimated with high accuracy. However, we need to address that comprehensive treatment of impact of bulk flow on the estimation of statistics of momentum is actually connected with the so called integral constraint problem, which is not considered here, appropriate proposals to correct effects of bulk flow are left for future investigation.

To overcome the huge variances in power spectra at large scales due to the limited number of Fourier modes, momentum power spectra of the initial cosmic fields at $z = 80$ of the simulation are measured and linearly evolved to specified redshifts, which are then used as linear templates to normalize measurements at those redshifts. The method greatly reduce the sample variances at large scales, making the comparison with theoretical models much smoother and clearer. Analysis of subsamples of our simulation shows that, cosmic variances of P_p, P_{θ_p} and $P_{\delta\theta_p}$ are at $\sim$20% level at large scales of $k < 0.1\ h$ Mpc^{-1}, being

much larger than the cosmic variances of the density power spectrum. In the nonlinear regime, cosmic variances of P_p and P_{θ_p} keep at the same level, but the cosmic variances of $P_{\delta\theta_p}$ gradually decrease to $\sim$10% at $k > 0.2\ h$ Mpc^{-1}. A quick comparison of momentum power spectra of dark matter in simulation with theories indicates that if precision requirement is set to $\sim$10%, at large scales the one loop SPT agrees with simulation slightly better than the linear theory at $z = 0$. Of course, the performance of one loop SPT improves with increasing redshifts.

We also notice that P_p contains strong power from the rotational part of momentum, and there is a considerably large stochastic component in θ_p which is completely not correlated with the density fluctuation. The two ingredients make it rather challenging to reconstruct the full momentum field and its divergence beyond linear regime with the information offered by the density and the cross correlation between density and momentum divergence, the three kinds of momentum power spectra have their own distinctness.

Acknowledgements JP is supported by the National Key R&D Program of China (Grant No. 2018YFE0202900), and the National Natural Science Foundation of China (Grant No. 11573030). It is greatly appreciated that Dr. Li Ming realized the simulation used in this work, and Dr. Feng Longlong kindly provided his code for reference.

Appendix A: PREDICTION OF EULERIAN PERTURBATION THEORY AT ONE LOOP LEVEL ON MOMENTUM POWER SPECTRA

The momentum power spectrum in Fourier space can be expressed as

$$P_p = P_v + \frac{1}{(2\pi)^3}\left[P \otimes P_v + P_{\delta v} \otimes P^*_{\delta v}\right] + 2\mathcal{B}_{\delta vv} + \mathcal{T}_{\delta v\delta v}\ , \tag{A.1}$$

where $P_v(k)$ is the power spectrum of peculiar velocity, $P(k)$ is the matter power spectrum (sometimes denoted as P_δ), $P_{\delta v}$ is the anisotropic cross-power spectrum of density contrast and peculiar velocity. In Equation (A.1) $\mathcal{B}_{\delta vv}$ and $\mathcal{T}_{\delta v\delta v}$ are integrations over bispectrum and trispectrum respectively

$$\mathcal{B}_{\delta vv} = \frac{1}{(2\pi)^3}\int B_{\delta vv}(\boldsymbol{k}-\boldsymbol{q},\boldsymbol{q},-\boldsymbol{k})\mathrm{d}\boldsymbol{q}$$
$$\mathcal{T}_{\delta v\delta v} = \frac{1}{(2\pi)^6}\int\int T_{\delta v\delta v}(\boldsymbol{k}-\boldsymbol{q},\boldsymbol{q},-\boldsymbol{k}-\boldsymbol{q}',\boldsymbol{q})\mathrm{d}\boldsymbol{q}\mathrm{d}\boldsymbol{q}'\ , \tag{A.2}$$

where $B_{\delta vv}(\boldsymbol{k}_1,\boldsymbol{k}_2,\boldsymbol{k}_3)\delta_D(\sum_i \boldsymbol{k}_i = 0) \equiv \langle\delta_1\boldsymbol{v}_2\cdot\boldsymbol{v}_3\rangle_c$, $T_{\delta v\delta v}(\boldsymbol{k}_1,\boldsymbol{k}_2,\boldsymbol{k}_3,\boldsymbol{k}_4)\delta_D(\sum_i \boldsymbol{k}_i = 0) \equiv \langle\delta_1\boldsymbol{v}_2\cdot\delta_3\boldsymbol{v}_4\rangle_c$, δ_D is the Dirac δ-function, and $\langle\ldots\rangle_c$ refers to the irreducible correlation.

At scales $k \ll 1\ h\,\mathrm{Mpc}^{-1}$ power spectrum of the curl component of velocity is an order of magnitude lower than the irrotational part (e.g., Pueblas & Scoccimarro 2009; Zheng et al. 2013), the velocity field can be approximated by the potential $\theta \equiv -\nabla\cdot\boldsymbol{v}/(Haf)$ alone. In such ansatz there are

$$P_{\delta v} = -i(Haf\boldsymbol{k}/k^2)P_{\delta\theta}\ ,\quad P_v = (Haf/k)^2 P_{\theta\theta}\ ,$$
$$B_{\delta vv}(\boldsymbol{k}-\boldsymbol{q},\boldsymbol{q},-\boldsymbol{k}) = (Haf)^2\frac{\boldsymbol{k}\cdot\boldsymbol{q}}{k^2q^2}B_{\delta\theta\theta}\ ,$$
$$T_{\delta v\delta v}(\boldsymbol{k}-\boldsymbol{q},\boldsymbol{q},-\boldsymbol{k}-\boldsymbol{q}',\boldsymbol{q}') = -(Haf)^2\frac{\boldsymbol{q}\cdot\boldsymbol{q}'}{q^2q'^2}T_{\delta\theta\delta\theta}\ , \tag{A.3}$$

where $f \equiv \mathrm{d}\ln D(z)/\mathrm{d}\ln a$ with $D(z)$ being the linear density growth factor at redshift $z = 1/a - 1$. The corresponding approximation to Equation (A.1) is then

$$\left(\frac{k}{Haf}\right)^2 P_p = P_{\theta\theta} + \frac{k^2}{(2\pi)^3}\left[P\otimes\left(\frac{P_{\theta\theta}}{k^2}\right) + \left(\frac{\boldsymbol{k}P_{\delta\theta}}{k^2}\right)\otimes\left(\frac{\boldsymbol{k}P_{\delta\theta}}{k^2}\right)\right] + k^2\left(2\mathcal{B}_{\delta\theta\theta} + \mathcal{T}_{\delta\theta\delta\theta}\right)\ , \tag{A.4}$$

where

$$\mathcal{B}_{\delta\theta\theta} = \frac{1}{(2\pi)^3}\int\frac{\boldsymbol{k}\cdot\boldsymbol{q}}{k^2q^2}B_{\delta\theta\theta}(\boldsymbol{k}-\boldsymbol{q},\boldsymbol{q},-\boldsymbol{k})\mathrm{d}\boldsymbol{q},$$
$$\mathcal{T}_{\delta\theta\delta\theta} = \frac{1}{(2\pi)^6}\int\int\frac{\boldsymbol{q}\cdot\boldsymbol{q}'}{q^2q'^2} \times T_{\delta\theta\delta\theta}(\boldsymbol{k}-\boldsymbol{q},\boldsymbol{q},-\boldsymbol{k}-\boldsymbol{q}',\boldsymbol{q}')\mathrm{d}\boldsymbol{q}\mathrm{d}\boldsymbol{q}'. \tag{A.5}$$

If δ and θ are both Gaussian, $\theta = \delta$, $B_{\delta\theta\theta} = 0$ and $T_{\delta\theta\delta\theta} = 0$, Equation (A.4) reduces to the known Gaussian approximation (e.g., Ma & Fry 2002),

$$\left(\frac{k}{Haf}\right)^2 P_p^G = P_L + \frac{k^2}{(2\pi)^3}\left[P_L\otimes\left(\frac{P_L}{k^2}\right) + \left(\frac{\boldsymbol{k}P_L}{k^2}\right)\otimes\left(\frac{\boldsymbol{k}P_L}{k^2}\right)\right]\ , \tag{A.6}$$

in which $P_L = D_z^2 P_0$ with P_0 being the linear power spectrum at $z = 0$, and $D_z = D(z)/D(z=0)$.

At large scales where nonlinearity is weak one can invoke perturbative theories, such as the standard Eulerian perturbation theory (SPT, Appendix B). Implementing the SPT power spectra (Appendix B.2) and bispectrum (Appendix B.3) to Equation (A.4), after truncation of terms

of order higher than D_z^4, yields

$$\begin{aligned}
&\left(\frac{k}{Haf}\right)^2 P_p^{(1)} = D_z^2 P_0 + D_z^4 (P_{\theta\theta,1} + P_{cov} + P_B),\\
&P_{cov} = P_{cov}^I + P_{cov}^{II},\ \ P_B = 2k^2 \mathcal{B}_{\delta\theta\theta,0},\\
&P_{cov}^I = \frac{k^2}{(2\pi)^3} P_0 \otimes \left(\frac{P_0}{k^2}\right),\\
&P_{cov}^{II} = \frac{k^2}{(2\pi)^3} \left(\frac{\boldsymbol{k} P_0}{k^2}\right) \otimes \left(\frac{\boldsymbol{k} P_0}{k^2}\right),
\end{aligned} \tag{A.7}$$

in which $\mathcal{B}_{\delta\theta\theta,0}$ is given by Equation (B.9), explicit formula to compute P_{cov} is in Appendix B.4.

The route leading to power spectrum of momentum divergence in SPT is different. The starting point is the continuity equation

$$a\frac{\partial \delta(\boldsymbol{x},t)}{\partial t} + \nabla\cdot\{[1+\delta(\boldsymbol{x},t)]\,\boldsymbol{v}(\boldsymbol{x},t)\} = 0\,. \tag{A.8}$$

Seljak (1996) has already utilized the equation to derive the power spectrum of the time derivative of the gravitational potential for investigation on the Rees-Sciama effect. Smith et al. (2009) also applied the same technique to measure the integrated Sachs-Wolfe effect in N-body simulation. Fourier transforming Equation (A.8) yields $\theta_p(\boldsymbol{k}) = \frac{1}{f}\partial\delta(\boldsymbol{k},a)/\partial\ln a$, corresponding power spectra are

$$\begin{aligned}
P_{\theta_p}(\boldsymbol{k}) &= \frac{1}{f^2}\langle \frac{\partial\delta(\boldsymbol{k},a)}{\partial\ln a}\frac{\partial\delta^*(\boldsymbol{k},a)}{\partial\ln a}\rangle,\\
P_{\delta\theta_p}(\boldsymbol{k}) &= \frac{1}{f}\langle \delta(\boldsymbol{k})\frac{\partial\delta^*(\boldsymbol{k},a)}{\partial\ln a}\rangle\,.
\end{aligned} \tag{A.9}$$

Inserting the expansion scheme of SPT (Eq. (B.1)), $\delta = \sum_n D_z^n \delta_{(n)}$, there is

$$\begin{aligned}
P_{\theta_p} &= D_z^2 P_0 + \sum_n D_z^{2n}\Big[2\sum_{j=1}^{n-1} j(2n-j)\langle\delta_{(j)}\delta^*_{(2n-j)}\rangle\\
&\qquad + n^2\langle\delta_{(n)}\delta^*_{(n)}\rangle\Big],\\
P_{\delta\theta_p} &= D_z^2 P_0 + \sum_n D_z^{2n}\Big[2\sum_{j=1}^{n-1} n\langle\delta_{(j)}\delta^*_{(2n-j)}\rangle\\
&\qquad + n\langle\delta_{(n)}\delta^*_{(n)}\rangle\Big],
\end{aligned} \tag{A.10}$$

where we have used the property that odd order terms are zero. The difference between P_{θ_p} or $P_{\delta\theta_p}$ and P lies in coefficients associated with terms at different orders, it is very convenient to calculate momentum power spectrum: once higher-order correction terms to P are ready, prediction of P_{θ_p} or $P_{\delta\theta_p}$ can be constructed simultaneously. P_{θ_p} and $P_{\delta\theta_p}$ to the order of D_z^4 are simply (Smith et al. 2009)

$$\begin{aligned}
P_{\theta_p}^{(1)} &= D_z^2 P_0 + D_z^4(6P_{13} + 4P_{22})\,,\\
P_{\delta\theta_p}^{(1)} &= D_z^2 P_0 + D_z^4(4P_{13} + 2P_{22})\,.
\end{aligned} \tag{A.11}$$

Appendix B: EXPANSION SCHEME AND COMPUTING FORMULAS

B.1. The Expansion

In SPT, δ_k and θ_k are expanded as

$$\delta_k = \sum_{n=1}^{\infty} D_z^n \delta_{(n)}\,,\quad \theta_k = \sum_{n=1}^{\infty} D_z^n \theta_{(n)}\,, \tag{B.1}$$

$\delta_{(1)} = \theta_{(1)}$ are simply linear quantities, higher order terms are constructed via

$$\begin{aligned}
\delta_{(n)} &= \frac{1}{(2\pi)^n}\\
&\times \int d^3q_1\ldots d^3q_n \delta_D(\sum_i \boldsymbol{q}_i - \boldsymbol{k}) F_n \delta_{(1)}(\boldsymbol{q}_1)\ldots\delta_{(1)}(\boldsymbol{q}_n),\\
\theta_{(n)} &= \frac{1}{(2\pi)^n}\\
&\times \int d^3q_1\ldots d^3q_n \delta_D(\sum_i \boldsymbol{q}_i - \boldsymbol{k}) G_n \delta_{(1)}(\boldsymbol{q}_1)\ldots\delta_{(1)}(\boldsymbol{q}_n).
\end{aligned} \tag{B.2}$$

The kernels F_n and G_n are homogeneous functions of wave vectors $\{\boldsymbol{q}_1,\ldots,\boldsymbol{q}_n\}$, of which explicit formulas can be found in Goroff et al. (1986) and Jain & Bertschinger (1994).

B.2. Power Spectra of δ and θ

Power spectra in the framework are organized in the form of

$$\begin{aligned}
P_{xy} &= \sum_{n=1}^{\infty} D_z^{2n} P_{xy,n-1},\\
P_{xy,n-1} &\equiv 2\sum_{j=1}^{n-1}\langle x_{(j)} y^*_{(2n-j)}\rangle + \langle x_{(n)} y^*_{(n)}\rangle,
\end{aligned} \tag{B.3}$$

where x, y represent δ or θ (for the δ–δ subscript is omitted by default in this paper), $P_{xy,0} = P_0$ is the linear matter power spectrum. Power spectrum corrected to 2-loop level is thus

$$\begin{aligned}
P_{xy}^{(2)} &= D_z^2 P_0 + D_z^4 P_{xy,1} + D_z^6 P_{xy,2}\\
&= P_{xy}^{(1)} + D_z^6 P_{xy,2},\\
P_{xy,1} &= 2P_{xy,13} + P_{xy,22},\\
P_{xy,2} &= 2P_{xy,15} + 2P_{xy,24} + P_{xy,33}\,,
\end{aligned} \tag{B.4}$$

in which explicit expressions of $P_{xy,ij} = \langle x_{(i)} y^*_{(j)}\rangle$ can be found in e.g., Bernardeau et al. (2002), Carlson et al. (2009) and Taruya et al. (2009). Then 1-loop corrections

to power spectra are

$$
\begin{aligned}
P_{13} &= \frac{P_0(k)}{504}\frac{k^3}{4\pi^2}\int_0^\infty \mathrm{d}r P_0(kr)\left[\frac{12}{r^2}-158+100r^2\right.\\
&\left.-42r^4+\frac{3}{r^2}(r^2-1)^3(7r^2+2)\ln\left|\frac{1+r}{1-r}\right|\right],\\
P_{\delta\theta,13} &= \frac{P_0(k)}{504}\frac{k^3}{4\pi^2}\int_0^\infty \mathrm{d}r P_0(kr)\left[\frac{24}{r^2}-202+56r^2\right.\\
&\left.-30r^4+\frac{3}{r^2}(r^2-1)^3(5r^2+4)\ln\left|\frac{1+r}{1-r}\right|\right],\\
P_{\theta\theta,13} &= \frac{P_0(k)}{168}\frac{k^3}{4\pi^2}\int_0^\infty \mathrm{d}r P_0(kr)\left[\frac{12}{r^2}-82+4r^2\right.\\
&\left.-6r^4+\frac{3}{r^2}(r^2-1)^3(r^2+2)\ln\left|\frac{1+r}{1-r}\right|\right],
\end{aligned}
\tag{B.5}
$$

and

$$
\begin{aligned}
P_{22} &= \frac{1}{98}\frac{k^3}{4\pi^2}\int_0^\infty \mathrm{d}r P_0(kr)\\
&\int_{-1}^1 \mathrm{d}x P_0\left(k\sqrt{1+r^2-2rx}\right)\cdot\frac{(3r+7x-10rx^2)^2}{(1+r^2-2rx)^2},\\
P_{\delta\theta,22} &= \frac{1}{98}\frac{k^3}{4\pi^2}\int_0^\infty \mathrm{d}r P_0(kr)\\
&\int_{-1}^1 \mathrm{d}x P_0\left(k\sqrt{1+r^2-2rx}\right)\\
&\cdot\frac{(3r+7x-10rx^2)(7x-r-6rx^2)}{(1+r^2-2rx)^2},\\
P_{\theta\theta,22} &= \frac{1}{98}\frac{k^3}{4\pi^2}\int_0^\infty \mathrm{d}r P_0(kr)\\
&\int_{-1}^1 \mathrm{d}x P_0\left(k\sqrt{1+r^2-2rx}\right)\cdot\frac{(7x-r-6rx^2)^2}{(1+r^2-2rx)^2}.
\end{aligned}
\tag{B.6}
$$

B.3. The Density-velocity-velocity Bispectrum

The loop expansion for the density-velocity-velocity bispectrum can be written down following Scoccimarro (1997) and Scoccimarro et al. (1998),

$$
B_{\delta\theta\theta} = D_z^4 B_{\delta\theta\theta,0} + D_z^6 B_{\delta\theta\theta,1} + \dots\,, \tag{B.7}
$$

in which the tree-level bispectrum is

$$
\begin{aligned}
B_{\delta\theta\theta,0}(\boldsymbol{k}_1,\boldsymbol{k}_2,\boldsymbol{k}_3) =\ & 2P_0(k_1)P_0(k_2)G_2(\boldsymbol{k}_1,\boldsymbol{k}_2)\\
&+2P_0(k_1)P_0(k_3)G_2(\boldsymbol{k}_1,\boldsymbol{k}_3)\\
&+2P_0(k_2)P_0(k_3)F_2(\boldsymbol{k}_2,\boldsymbol{k}_3)\,.
\end{aligned}
\tag{B.8}
$$

$\mathcal{B}_{\delta\theta\theta}$ as the integral of the bispectrum $B_{\delta\theta\theta}$ is therefore $\mathcal{B}_{\delta\theta\theta} = D_z^4\mathcal{B}_{\delta\theta\theta,0} + D_z^6\mathcal{B}_{\delta\theta\theta,1} + \dots$, and

$$
\mathcal{B}_{\delta\theta\theta,0} = I_1 + I_2 + I_3\,, \tag{B.9}
$$

where

$$
\begin{aligned}
I_1 &= -\frac{1}{7}\frac{k}{4\pi^2}\int_0^\infty \mathrm{d}r P_0(kr)\\
&\int_{-1}^1 \mathrm{d}x P_0\left(k\sqrt{1+r^2-2rx}\right)\frac{x(r-7x+6rx^2)}{1+r^2-2rx},\\
I_2 &= \frac{1}{7}\frac{k}{4\pi^2}P_0(k)\int_0^\infty \mathrm{d}r\\
&\int_{-1}^1 \mathrm{d}x P_0\left(k\sqrt{1+r^2-2rx}\right)\frac{r^3x(7rx-1-6x^2)}{1+r^2-2rx},\\
I_3 &= -\frac{2}{3}\frac{k}{4\pi^2}P_0(k)\int_0^\infty (r^2+1)P_0(kr)\mathrm{d}r\,.
\end{aligned}
\tag{B.10}
$$

B.4. Convolution Terms

$$
\begin{aligned}
P_{cov}^{I} &= \frac{k^3}{4\pi^2}\int_0^\infty \mathrm{d}r P_0(kr)\\
&\int_{-1}^1 P_0\left(k\sqrt{1+r^2-2rx}\right)\mathrm{d}x\,,\\
P_{cov}^{II} &= \frac{k^3}{4\pi^2}\int_0^\infty \mathrm{d}r P_0(kr)\\
&\int_{-1}^1 P_0\left(k\sqrt{1+r^2-2rx}\right)\frac{r(x-r)}{1+r^2-2rx}\mathrm{d}x\,.
\end{aligned}
\tag{B.11}
$$

References

Anselmi, S., & Pietroni, M. 2012, J. Cosmol. Astropart. Phys., 2012, 013

Bahcall, N. A., Cen, R., & Gramann, M. 1994, ApJL, 430, L13

Baldauf, T., Mercolli, L., & Zaldarriaga, M. 2015, Phys. Rev. D, 92, 123007

Bernardeau, F., Colombi, S., Gaztañaga, E., et al. 2002, Phys. Rep., 367, 1

Bernardeau, F., Crocce, M., & Scoccimarro, R. 2008, Phys. Rev. D, 78, 103521

Bernardeau, F., Crocce, M., & Scoccimarro, R. 2012, Phys. Rev. D, 85, 123519

Bernardeau, F., & van de Weygaert, R. 1996, MNRAS, 279, 693

Carlson, J., White, M., & Padmanabhan, N. 2009, Phys. Rev. D, 80, 043531

Carrasco, J. J. M., Foreman, S., Green, D., et al. 2014, J. Cosmol. Astropart. Phys., 2014, 057

Carrasco, J. J. M., Hertzberg, M. P., & Senatore, L. 2012, Journal of High Energy Physics, 9, 82

Chen, J., Zhang, P., Zheng, Y., et al. 2018, ApJ, 861, 58

Colombi, S., Chodorowski, M. J., & Teyssier, R. 2007, MNRAS, 375, 348

Colombi, S., Jaffe, A., Novikov, D., et al. 2009, MNRAS, 393, 511

Cooray, A., & Sheth, R. 2002, Phys. Rep., 372, 1

Crocce, M., & Scoccimarro, R. 2006a, Phys. Rev. D, 73, 063520
Crocce, M., & Scoccimarro, R. 2006b, Phys. Rev. D, 73, 063519
Crocce, M., & Scoccimarro, R. 2008, Phys. Rev. D, 77, 023533
Crocce, M., Scoccimarro, R., & Bernardeau, F. 2012, MNRAS, 427, 2537
Cui, W., Liu, L., Yang, X., et al. 2008, ApJ, 687, 738
Foreman, S., Perrier, H., & Senatore, L. 2016, J. Cosmol. Astropart. Phys., 2016, 027
Frigo, M., & Johnson, S. G. 2005, Proceedings of the IEEE, 93, 216
Giocoli, C., Bartelmann, M., Sheth, R. K., et al. 2010, MNRAS, 408, 300
Goroff, M. H., Grinstein, B., Rey, S.-J., et al. 1986, ApJ, 311, 6
Gorski, K. M., Davis, M., Strauss, M. A., et al. 1989, ApJ, 344, 1
Hiramatsu, T., & Taruya, A. 2009, Phys. Rev. D, 79, 103526
Howlett, C. 2019, MNRAS, 487, 5209
Jain, B., & Bertschinger, E. 1994, ApJ, 431, 495
Jing, Y. P. 2005, ApJ, 620, 559
Lesgourgues, J. 2011, arXiv:1104.2932
Li, M., Pan, J., Gao, L., et al. 2012, ApJ, 761, 151
Ma, C., & Fry, J. N. 2000, ApJ, 543, 503
Ma, C.-P., & Fry, J. N. 2002, Physical Review Letters, 88, 211301
Matarrese, S., & Pietroni, M. 2007, J. Cosmol. Astropart. Phys., 6, 26
Matarrese, S., & Pietroni, M. 2008, Modern Physics Letters A, 23, 25
McDonald, P. 2007, Phys. Rev. D, 75, 043514
Mead, A. J., Peacock, J. A., Heymans, C., et al. 2015, MNRAS, 454, 1958
Okumura, T., Seljak, U., Vlah, Z., et al. 2014, J. Cosmol. Astropart. Phys., 2014, 003
Park, C. 2000, MNRAS, 319, 573
Park, C.-G., & Park, C. 2006, ApJ, 637, 1
Park, H., Komatsu, E., Shapiro, P. R., et al. 2016, ApJ, 818, 37
Peebles, P. J. E. 1980, The Large-scale Structure of the Universe (Princeton, N.J., Princeton University Press)
Pietroni, M. 2008, J. Cosmol. Astropart. Phys., 10, 36
Pietroni, M., Mangano, G., Saviano, N., et al. 2012, J. Cosmol. Astropart. Phys., 1, 19
Pueblas, S., & Scoccimarro, R. 2009, Phys. Rev. D, 80, 043504
Qin, F., Howlett, C., & Staveley-Smith, L. 2019, MNRAS, 487, 5235
Scoccimarro, R. 1997, ApJ, 487, 1
Scoccimarro, R., Colombi, S., Fry, J. N., et al. 1998, ApJ, 496, 586
Scoccimarro, R., Sheth, R. K., Hui, L., et al. 2001, ApJ, 546, 20
Seljak, U. 1996, ApJ, 460, 549
Senatore, L., & Zaldarriaga, M. 2015, J. Cosmol. Astropart. Phys., 2015, 013
Smith, R. E., Hernández-Monteagudo, C., & Seljak, U. 2009, Phys. Rev. D, 80, 063528
Smith, R. E., et al. 2003, MNRAS, 341, 1311
Springel, V. 2005, MNRAS, 364, 1105
Sugiyama, N. S., & Futamase, T. 2012a, ApJ, 760, 114
Sugiyama, N. S., & Futamase, T. 2012b, arXiv:1210.7499
Sugiyama, N. S., Okumura, T., & Spergel, D. N. 2016, J. Cosmol. Astropart. Phys., 2016, 001
Takahashi, R., Sato, M., Nishimichi, T., et al. 2012, ApJ, 761, 152
Taruya, A., Bernardeau, F., Nishimichi, T., et al. 2012, Phys. Rev. D, 86, 103528
Taruya, A., & Hiramatsu, T. 2008, ApJ, 674, 617
Taruya, A., Nishimichi, T., Saito, S., & Hiramatsu, T. 2009, Phys. Rev. D, 80, 123503
Valageas, P. 2008, A&A, 484, 79
Wang, Y., Rooney, C., Feldman, H. A., et al. 2018, MNRAS, 480, 5332
Yang, Y.-B., Feng, L.-L., Pan, J., et al. 2009, RAA (Research in Astronomy and Astrophysics), 9, 227
Yu, Y., Zhang, J., Jing, Y., et al. 2015, Phys. Rev. D, 92, 083527
Zheng, Y., Zhang, P., Jing, Y., et al. 2013, Phys. Rev. D, 88, 103510